

Flares in Open Clusters with K2.

II. M35, Hyades, and Ruprecht 147

Ekaterina Ilin¹, Sarah J. Schmidt¹, Katja Poppenhäger¹, James R. A. Davenport² and Klaus G. Strassmeier¹

¹ Leibniz Institut für Astrophysik Potsdam

e-mail: eilin@aip.de

² University of Washington e-mail: jrad@uw.edu

Received XXX; accepted XXX

ABSTRACT

Context. Flares can help us trace magnetic activity because are bright and high-contrast on low mass stars.

Aims. This study aims to quantify flaring activity on these stars as a function of mass and age.

Methods. We automatically detected flares in K2 time-domain photometry, using the open-source software K2SC to remove instrumental and astrophysical variability from K2 light curves. We used injection and recovery of synthetic flares to assess detection thresholds, time sampling and de-trending effects on the inferred flare energies. With additional data from the full K2 archive we added stars with a larger variety of ages and spectral types to the analysis of the previous study (Ilin et al. 2019). We compared previous results from the Pleiades and Praesepe to the flare frequency distributions (FFDs) in M35 and the Hyades, respectively. Ruprecht 147 filled in the age gap at 2.5 Gyr between the aforementioned young clusters and the solar age cluster M67.

Results. We find that the flare production mechanism is similar for the entire parameter space, following a power law relation with exponent $\alpha \approx 2$, but the flaring frequencies depend on both mass, and age. We discuss X and Y.

Key words. Methods: data analysis, Stars: activity, Stars: flare, Stars: low-mass

Use \titlerunning to supply a shorter title and/or \authorrunning to supply a shorter list of authors.

1. Introduction

Flares are explosions on stellar surfaces with a complex spatio-temporal and energetic phenomenology. We know that flares are magnetic re-connection events that lead to a change in field line topology and subsequent energy release (Priest & Forbes 2002). We can observe flares in nearly all electromagnetic bands, from radio to X-rays, and on all stars that possess a convection zone. From late F type stars to ultracool dwarfs (Gizis 2013). But even with continuous monitoring at high temporal resolution, the random occurrence of solar flares makes them costly observing targets, especially in coordinated multi-band observations. In integrated light, most solar flares have a far too low contrast and intensity to be observable. Stellar flares on cool stars have two advantages in this respect. They are often bright, enhancing stellar flux by up to several orders of magnitude, and they typically exhibit blackbody emission at temperatures significantly higher than their stars' photospheres. With the evidence that the physical processes that cause flares on the Sun and other stars are the same (Karoff 2016), solar and stellar flares can inform each other (Shibayama et al. 2013). Inconsistencies in extrapolations from solar to stellar conditions (Aarnio et al. 2011; Aarnio et al. 2012; Drake et al. 2012; Alvarado-Gómez et al. 2018). Large surveys like Kepler and TESS enable statistical flare studies of stars that were not pre-selected for their activity (Walkowicz et al. 2011). Statistical studies of stellar flaring activity can help us understand the underlying physical processes CITE stellar surface magnetic fields, starspots (Davenport 2015; Howard

et al. 2019b), how flares relate to stellar angular momentum evolution (Mondrik et al. 2019; Howard et al. 2019b), how they affect the atmospheres of exoplanets (Lecavelier des Etangs et al. 2012; Loyd et al. 2018; Tilley et al. 2019; Howard et al. 2019a), and inform galactic archaeology (Howard et al. 2019a). Basic parameters that affect flaring behaviour on stars are their masses, and ages. Ages can be controlled for in coeval groups of stars, and flaring-age studies in binaries showed consistency in activity for both components in the majority of targets (Lurie et al. 2015; Clarke et al. 2018). Open clusters present other coeval groups of stars with well-determined ages. Ilin et al. (2019) (hereafter PaperI) investigated the flaring activity of late-K to mid-M dwarfs in three open clusters (OCs), the Pleiades, Praesepe, and M67, using K2 time domain photometry. They analysed the flare frequency distributions (FFDs), with respect to different masses and cluster ages. For the cluster members, the light curves revealed that their flaring activity declines both with age and mass. The decline is faster for higher mass stars. Recently, Davenport et al. (2019) put forward an empirical parametrization of this flaring-mass-age relation based on FFDs. The present study aims to extend the results in PaperI to the age of Ruprecht 147 (2.5 Gyr), and both higher and lower masses than in the previous study. We also test the previous results from the Pleiades on M35, and the results from Praesepe on the Hyades, as both OC pairs have approximately the same ages. Because the Kepler satellite retired in fall 2018, we can now use the complete K2 data set, and supplement all three OCs in PaperI with additional light curves. Additionally, we use high quality K2 light curves available for M67 (Nardiello et al. 2016) and M35 (Soares-Furtado et al. 2017). We discuss our results with

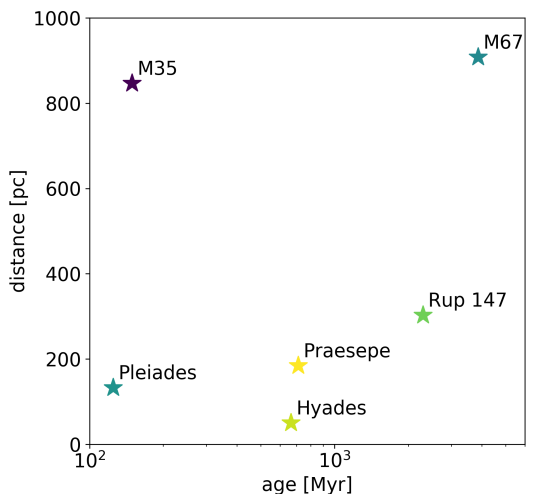


Fig. 1. The values for age, metallicity, and distance are approximate values from a compilation of existing literature, see Appendix B.1.

respect to potential breaks in the power law distribution at high energies. Finally, we use the results to test the parametrizability in Davenport et al. (2019).

2. Data

Our main data are K2 target pixel files that were provided by the Kepler archives hosted at MAST, and light curves derived from them (Aigrain et al. 2016; Soares-Furtado et al. 2017; Vinícius et al. 2018). To assign T_{eff} to the targeted stars we used multi-band photometry obtained from Tycho, UCAC4, 2MASS, Pan-STARRS, and Gaia catalogs. To assign ages to the targeted stars OC membership information was compiled from the literature. An overview over the cluster sample is presented in Table ?? and illustrated in Figure 1.

2.1. K2 light curves

The Kepler (Koch et al. 2010) spacecraft finished its follow-on mission K2 (Howell et al. 2014) in September 2018, after having completed nearly 20 80-day observing campaigns. Even though Kepler and K2 data are used in more than 2 400 publications to date, the public archive can still be considered understudied (Bastien et al. 2018). In this spirit we took up the analysis of about 4 000 Kepler target pixel files that each contain up to 80 days of 30 min cadence observations in white light ($4, 200 - 9, 000 \text{ \AA}$). We also used light curves extracted from the K2 C0 super stamp. A super stamp is an aggregated set of typical Kepler postage stamps placed over a densely populated field, that also covers M35 (Soares-Furtado et al. 2017).

As K2 was conducted on the two-wheeled Kepler satellite, it was subjected to substantial drift motion (spacecraft roll, Van Cleve et al. 2016) and had an overall reduced pointing accuracy. To mitigate these effects, various solutions were developed (Vanderburg & Johnson 2014; Aigrain et al. 2016; ?; Luger et al. 2018)

2.2. Membership matching

We obtained membership information from multiple catalogs for each cluster. We cross-matched these catalogs on RA and

declination within 3 arcsec. The resulting target lists were used to search the K2 archive, or were matched to the catalogs of extracted light curves from crowded fields in the case of M35 (Soares-Furtado et al. 2017) and M67 (Nardiello et al. 2016).

One part of the membership catalogs provided membership probabilities (Douglas et al. 2014; Bouy et al. 2015; Cantat-Gaudin et al. 2018; Olivares et al. 2018; Reino et al. 2018; Gao 2018; Olivares et al. 2019). For the other part no probability was provided (Rebull et al. 2016a; Douglas et al. 2017; Gaia Collaboration et al. 2018a), or qualitative classifiers were given (Curtis et al. 2013; Gonzalez 2016; Rebull et al. 2017). In the latter cases we assigned approximate probabilities anchored to the set threshold for inclusion into our final sample. Absence in a catalog did not decrease the likelihood of membership, as each catalog shows different selection biases which we did not address in this study. We set the threshold mean membership probability p for a target in our sample to 0.8.

2.3. Open Clusters

We studied flaring activity in the low mass stars in six open clusters spanning from ZAMS to solar age. Table 1 provides an overview over the final sample. The literature overview of age, distance, and metallicity determinations is given in Table ?? in the Appendix. Membership probability histograms of the final sample are displayed in Figure ??.

2.3.1. Pleiades

The Pleiades, a nearby ZAMS cluster, were observed in Campaign 4, and were treated in PaperI. We include the cluster in this work for completeness and to illustrate improvements to (PaperI). We revisited the memberships from Rebull et al. (2016a), which were your in the previous work, and merged them with lists of members determined by Olivares et al. (2018); Gaia Collaboration et al. (2018a); and Cantat-Gaudin et al. (2018).

2.3.2. M35

M35 is a ZAMS cluster 900 pc away, observed during Campaign 0 in K2. We merged membership lists from Cantat-Gaudin et al. (2018); Gaia Collaboration et al. (2018a); and Bouy et al. (2015). There are only five K2 light curves, but we identified multiple additional members with publicly available¹ light curves obtained from Soares-Furtado et al. (2017). They used an image subtraction technique in the campaign's super stamps, a self flat-fielding de-trending inspired by K2SFF (Vanderburg & Johnson 2014), and a trend-filtering algorithm developed by Kovács et al. (2005). We preferred PSF photometry in cases where both aperture K2 and PSF LCs were available. We took the raw extracted PSF light curves and de-trended them using K2SC.

2.3.3. Hyades

The Hyades are a 0.6 Gyr old OC observed during Campaigns 4 and 13 with K2. It is about as old as Praesepe. We merged membership tables obtained from Douglas et al. (2014); Reino et al. (2018); and Gaia Collaboration et al. (2018a).

¹ <https://k2.hatsurveys.org/archive/>

Table 1. Open clusters.

cluster	<i>n</i>	LCs	SLCs	LLCs	PSF LCs	age[Myr]	distance[pc]	[Fe/H]
Pleiades	2033	944	33	911	0	125		
M35	1614	5	0	5	158			
Hyades	655	301	42	259	0			
Praesepe	1281	2500	68	2432	0			
Rup 147	213	97	25	72	0			
M67	1344	1141	118	1023	1019			

Notes. *n* is the approximate number of members with $p > 0.8$. LCs, SLCs, LLCs, and PSF LCs denote the number of available light curves, short cadence light curves, long cadence light curves, and PSF de-detrended light curves, respectively. The values for age, [Fe/H], and distance are approximate values from a comparison of existing literature, detailed in Appendix B.1.

149 2.3.4. Praesepe

150 Praesepe appeared in Campaign 5, and was previously treated
151 in PaperI. It was then observed again during Campaign 13. We
152 revisited the memberships obtained by Douglas et al. (2014), and
153 matched them to the members identified in Douglas et al. (2017)
154 Rebull et al. (2017); Cantat-Gaudin et al. (2018); and Gaia Col-
155 laboration et al. (2018a).

191 used the average extinction value of the respective cluster. We
192 accounted for extinction in Gaia BP and RP using the reddening
193 $E(B_P - R_P)$ derived from Gaia photometry and parallax from
194 Gaia DR2 (Andrae et al. 2018). We dropped targets that were
195 too bright (Kepler magnitude $K_p \leq 9$).
196

197 2.3.5. Ruprecht 147

198 Ruprecht 147 is a 2.5 Gyr old OC observed during Campaign 5
199 with K2. We used the mean membership probabilities obtained
200 from a number of studies (Curtis et al. 2013; Cantat-Gaudin et al.
201 2018; Olivares et al. 2019) combined with the members found
202 by Gaia Collaboration et al. (2018a) to identify the most likely
203 members.

204 2.4.2. Effective temperatures

205 2.3.6. M67

206 M67 is a solar-age, solar metallicity OC about 900 pc away.
207 Multiple members were observed during Campaign 5, and 208 visited in Campaigns 16 and 18. We did not find any flares 209 in M67 in Campaign 5 (PaperI) observing the members identified
210 by Gonzalez (2016). The recent campaigns brought both ad-211
212 tional observations, and entirely new targets to the sample. We
213 merged the members from Gonzalez (2016) with a recent study
214 based of Gaia DR2 data (Gao 2018). Additionally, we obtained
215 PSF-detrended light curves for Campaign 5 from Nardiello et al.
216 (2016).

217 We applied several methods and color-temperature relations
218 (CTRs) to determine robust T_{eff} . We used CTRs from Boyajian et al. (2013) and Mann et al. (2016) (erratum to Mann et al. 219 2015), and T_{eff} derived from Gaia DR2 using the StarHorse algorithm (Queiroz et al. 2018) and inferred from Gaia DR2 using the Apsis pipeline (Bailer-Jones et al. 2013; Andrae et al. 2018).
220 Boyajian et al. (2013) determined CTRs from a range of inter-221
222 ferometrically characterized stars using $g - z$, $g - i$, $g - r$,
223 $g - J$, $g - H$, and $g - K$ colors from SDSS and Johnson magni-224
225 tudes for A to K stars. Their sample is centered on solar metal-226
227 licity, so we constrained the use of these CTRs to stars with
228 $-0.25 < [\text{Fe}/\text{H}] < 0.25$. We transformed 2MASS JHK to $J - H$,
229 $H - K$, and $J - K$ in the Johnson system as the authors from
230 2MASS to the Bessell-Brett system (Carpenter 2001), and from
231 Bessell-Brett to Johnson using the relations in Bessell & Brett
232 (1988).

233 Mann et al. (2015) provide CTRs from absolutely calibrated
234 spectra to which they fitted atmospheric models to obtain T_{eff} .
235 Alternatively, they determined T_{eff} from long-baseline optical
236 interferometry measurements using the bolometric flux. Among
237 others, they note transformations for SDSS/2MASS $r - z$ and
238 $r - J$, or Gaia $BP - RP$ where extra information can be added
239 from metallicity or 2MASS $J - H$. The relations in Mann et al.
240 (2015) are only valid if metallicity is sufficiently close to solar,
241 which is satisfied for all clusters in this paper (see Table ??).
242 M35 may be an exception to this rule.

243 We supplemented our estimates with T_{eff} estimates from Anders
244 et al. (2019) who used the StarHorse pipeline (Queiroz et al.
245 2018) on Gaia DR2.

246 Gaia DR2 published effective temperatures for over 160 million
247 sources (Gaia Collaboration et al. 2018b). The typical uncer-
248 tainty is quoted at 324 K, but it is lower for stars above ~ 4100
249 K and below ~ 6700 K, so that we adopt 175 K which is above
250 the quoted root-median-squared error in this T_{eff} range (Andrae
251 et al. 2018), and use provided values only in this range.

252 Empirical CTRs suffer from systematic errors that stem both
253 from the different methods applied, and from sample selection
254 biases. We used as many empirical relations as possible in their
255 appropriate ranges to obtain multiple T_{eff} estimates from which
256 we then drew a more reliable median value. Targets that were
257

258 2.4. Effective temperatures, stellar radii, and luminosities

259 2.4.1. Photometry and extinction correction

260 We determined effective temperatures T_{eff} using broadband
261 photometry the Two Micron All Sky Survey (2MASS; Skrutskie
262 et al. 2006), the Panoramic Survey Telescope and Rapid
263 Response System (Pan-STARRS) Data Release 1 (Chambers et al.
264 2016), and Gaia DR2 (Gaia Collaboration et al. 2018b). We
265 applied quality cuts to 2MASS, Pan-STARRS DR1, and Gaia DR2
266 data, as described in Appendix C, and removed foreground
267 stars using Gaia DR2 parallaxes. We corrected the 2MASS
268 and PanSTARRS photometry in M35, M67, and Ruprecht
269 147 for extinction using the most recent version (Green et al.
270 2019) of the dustmaps package that provides 3D dust maps
271 derived from 2MASS and PanSTARRS photometry together
272 with Gaia distances (Green et al. 2018). If there was no
273 parallax available we used the cluster median distance instead.
274 If an extinction value was not available for a given star
275

lacking sufficient photometric data to derive T_{eff} , or were too hot to be expected to have a convective envelope ($T_{\text{eff}} \geq 7000$ K), were flagged accordingly, and removed from the sample. We dropped all targets where the uncertainty on the weighted mean T_{eff} was greater than 10%. Only targets that were assigned a T_{eff} were searched for flares.

2.4.3. Stellar radii

We used a catalog of empirically characterised stars (Yee et al. 2017) to derive R_* from T_{eff} (Fig. 4). Yee et al. (2017) collected 404 stars with high-resolution spectra from the literature, and own observations of mid to late K-dwarfs, spanning low mass stars from 7000 K down to 3000 K. For these stars, the resulting catalog is accurate to 100 K in T_{eff} , 15 % in R_* , and 0.09 dex in [Fe/H]. We interpolated between stars from the catalog to our derived T_{eff} , and propagated the resulting scatter to the uncertainty in R_* if $T_{\text{eff}} > 3500$ K. For stars with $T_{\text{eff}} < 3500$ K we used $T_{\text{eff}} - R_*$ relations derived by (Mann et al. 2015, 2016).

2.4.4. Spectra

We assigned spectra to our targets from the SpecMatchEmp Yee et al. (2017) and the FlareSpecPhot libraries (Schmidt 2014; Kirkpatrick et al. 2010; Burgasser et al. 2007, 2008, 2010, 2004; Cruz et al. 2004; Burgasser & McElwain 2006; Rayner et al. 2009; Doi et al. 2010; Filippazzo et al. 2015; Cruz et al. 2003; West et al. 2011; Bochanski et al. 2010, 2007; Schmidt et al. 2010, 2015, 2014; Mann et al. 2015). When a spectrum was available for the derived spectral type in FlareSpecPhot, we preferred it over SpecMatchEmp, which was the case for all stars cooler than M0, where we mapped spectral type to effective temperature as appears in Pecaut & Mamajek (2013). We then combined stellar radii R_* , T_{eff} , and spectra to projected bolometric luminosities $L_{\text{bol},*}$, and projected luminosities in the Kepler band $L_{Kp,*}$ (Shibayama et al. 2013; Ilin et al. 2019). Uncertainties $L_{Kp,*}$ ranged from 9 % to 52 % with a median value of 17 %.²⁹⁴

3. Methods

We detected flare candidates automatically, and validated the by eye. We attempted to assign recovery probabilities and corrected for sampling effects using injection/recovery tests but the procedure was not scalable due to computational costs. We performed injection recovery on a handful of example light curves to see that de-trending and intrinsic light curve properties smear out the ED recovery with varying distributions that add an uncertainty of about 30%. Most of the candidates are expected to have a complex shape that deviates from the classical flare template. The validation yielded an estimate on the uncertainty on the energy released in the Kepler band. The frequency distribution of these flare energies are believed to follow a power law that spans multiple orders of magnitude. We adopted this model, and used two different Maximum Likelihood estimators to obtain the power law exponents. We tested the best fit parameters with the Kolmogorov-Smirnov test, and probed possible truncation of the power law relation with an exceedance test.

3.1. Flare finding

We used the open source software AltaiPony² to automatically detect and characterize flares in our sample. The code base

lies on K2SC³ (Aigrain et al. 2016) to remove instrumental and astrophysical variability from K2 light curves. We did not use the pre-detrended light curves available on MAST, but used K2SC to derive our own, because we clipped outliers at 3σ iteratively, as compared to the original work, where outliers were clipped at 5σ (Aigrain et al. 2016).

After de-trending, the flare finder algorithm looked for continuous observing periods, defined as being longer than 10 data points at a minimum cadence of 2 h. All further routines were run on these observing periods. The finder iteratively clipped excursions from the median value at 3σ rolling window noise above median plus uncertainty given from K2SC de-trending. After each iteration, outliers were cut down to the current median value. Either after convergence, or 50 iterations, the resulting median value was adopted. With this median as quiescent flux, flare candidates were identified with the same procedure as during the median value calculation, but now we additionally required at least three consecutive data points to fulfil the σ -criterion. Flare candidates were merged into single candidate events if they were no more than three data points apart. For each of these candidates occurrence time, amplitude and equivalent duration (ED) was returned.

The Kepler flare sample has shown to be difficult to treat in a fully automated way. Without manual vetting, the event samples remain significantly contaminated (Yang & Liu 2019).

ED is the area between the LC and the quiescent flux, that is, the integrated flare flux divided by the median quiescent flux F_0 of the star, integrated over the flare duration (Hunt-Walker et al. 2012):

$$ED = \int dt \frac{F_{\text{flare}}(t)}{F_0}. \quad (1)$$

ED is a quantity independent of calibration and distance that is suited to compare flaring activity on stars where these properties are uncertain. It describes the time during which a star releases as much energy as the flare itself. This time can be shorter or longer than the actual flare duration.

The uncertainty in ED depends on the light curve noise properties, time sampling, and other intrinsic characteristics. Moreover, K2SC de-trending and the flare finding procedure introduce additional uncertainty that dominates the photometric noise. Carrying out injection and recovery that takes into account the effect of GP regression that underlies K2SC. We only performed injection-recovery on a small number of light curves with flares to estimate the .

3.2. Kepler flare energies

(see PaperI for details).

Multiband time resolved observations of active M dwarfs have shown that continuum flux accounts for the majority of the energy radiated by flares (Kowalski et al. 2013). The effective temperature of this blackbody, however, varies by a great degree, with, to date, no robust predictor of that temperature:

While solar flares are relatively cool, with $T_{\text{eff}} \approx 5000 - 7000$ K (Kleint et al. 2016; Kerr & Fletcher 2014; Watanabe et al. 2013; Namekata et al. 2017), SEDs of stellar flares tend to be blue (?). At least one M dwarf flare reached 40 000 K as seen in FUV spectra (Froning et al. 2019), and most events exhibit temperatures of about 9 000 – 10 000 K (Hawley & Fisher 1992; Kretzschmar 2011; Shibayama et al. 2013). A dependence of flare temperature on

² <https://github.com/ekaterinailin/AltaiPony>

³ <https://github.com/OxEs/k2sc>

318 stellar age, or mass, or both, will enter our analysis if we attempt
 319 to quantify bolometric flare energy. At about 6 200 K, the Kepler
 320 pass band captures the largest flux fraction, at 10 000 K 72 %,
 321 at 40 000 K only 4% of this value is transmitted. Another effect
 322 is that flares of equal flare energy but hotter SED would not be
 323 seen in the Kepler band at all.
 324 We propagated the uncertainties σ_{ED} and σ_L (on $L_{*,Kp}$) in
 325 quadrature to $E_{Kp,\text{flare}}$.
 326

327 3.3. Power law fits

328 Flare frequency distributions follow power law relations that
 329 cover several orders of magnitude, from solar microflares to
 330 stellar superflares. We fitted power law functions to the FFDs using
 331 three different approaches.
 332 The first method was a maximum likelihood estimator
 333 (MLE) (Maschberger & Kroupa 2009). As recommended
 334 by Maschberger & Kroupa (2009), we applied the stabilized
 335 Kolmogorov-Smirnov (KS) test at 95 % significance level to all
 336 power law fits in the sample. If the test fails the power law model
 337 does not fit the data at the given significance level. If the test
 338 passes, this does not give any information whether the power
 339 law model is the correct assumption. The goodness of fit can
 340 be estimated from the visual inspection of percentile-percentile
 341 plots, given in the online material⁴. We used the KS test itera-
 342 tively to determine the FFDs' low-energy cutoff ED_{\min} for the
 343 power law distribution. This cutoff does not reflect the physical
 344 threshold for criticality because the cutoff is seen at lower ener-
 345 gies in similar stars with higher sensitivity, for example, higher
 346 candence. The cutoff also does not directly imply that flare can-
 347 didates detected above or below the cutoff are more or less likely
 348 to be detected because the flare detection probability is a func-
 349 tion of both duration and amplitude, and not only of energy.
 350 Above all, it is not straightforward to account for the deviation
 351 from an ideal power law at low energies, because the aforemen-
 352 tioned effects may be partly cancelled by background contam-
 353 ination from, for instance, cosmic rays (?). We believe that we
 354 are mostly limited by the non-linear dependence for the energy
 355 bias from time sampling effects (?) and recovery probability on
 356 flare duration and amplitude. These parameters are not resolved
 357 in FFDs, and while they are correlated there is significant spread
 358 in the duration-amplitude relation to blur the cutoff in the FFD.
 359 One way to account for this circumstance is to inject and recover
 360 synthetic flares with a variety of durations and amplitudes and to
 361 determine energy ratios and recovery probabilities for each in-
 362 dividual candidate, assuming that the underlying flare shape can
 363 be sufficiently well parametrized, as was done in Davenport et al.
 364 (2014)

365 The second method used the MLE result as a prior for α . Follow-
 366 ing Wheatland (2004), we defined the joint posterior distribution
 367 for the probability ϵ that a flare with ED or energy above some
 368 value S_2 occurs within a time period ΔT :

$$p(\epsilon, \alpha) = C \cdot (-\ln(1 - \epsilon))^M \cdot (\alpha - 1)^M \cdot \Gamma(\alpha) \left[\frac{(S_2/S_1)^{M+1}}{\pi} \right]^\alpha \cdot (1 - \epsilon)^{(T/\Delta T) \cdot (S_2/S_1)^{\alpha-1} - 1}. \quad (2)$$

369 C is the normalisation constant, M is the number of events,
 370 the total observation time. Γ contains the prior distribution for α

and S_1 denotes the detection threshold above which all flares are
 detected. π encapsulates the flare energies as

$$\pi = \prod_{i=1}^M \frac{s_i}{S_1} \quad (3)$$

, where $\{s_1, s_2, \dots, s_m\}$ are the flare energies or ED .

The posterior distribution in Wheatland (2004) captures both the Poissonian distribution of flare events in time, and their power law distribution in energy, simultaneously. Wheatland (2004) derived this model to be able to predict the flaring rate of a given active region on the sun, and offered an extension to Eq. 2 that treated changing flaring activity rates as the active region evolves, and also characteristics of the active region itself, such as sunspot classifiers. In our simplification of the model, we assumed that the flare generating process did not change within the observation time span in any star in our sample ($M = M'$ in Eq. 24 in Wheatland (2004)). Another assumption was that this process was the same for all stars in the sample ($\Lambda_{MC} = 1$ in Eq. 24). Under these assumptions the information gained from the light curves could be stacked together.

With a uniform prior for α the results from the MLE and Markov Chain Monte Carlo (MCMC) sampling from the posterior distribution are the same, the latter allowed us to fit for ϵ and α simultaneously. Another advantage of the latter approach is that we could use more informative priors.

We chose our prior to reflect the power law exponent results discussed in the literature. The studies we took into account analysed flare frequency distributions of stellar flares in the optical regime, and focused mostly on K and M dwarfs (Lurie et al. 2015; Howard et al. 2019a; ?; ?) or ultra-cool dwarfs (?) but also solar-type stars (Shibayama et al. 2013). We also used a Gaussian fit to α obtained from the posterior distribution using the full sample of flares as the prior for a subsequent Bayesian analysis of individual age and T_{eff} bins. Assuming that α is universal for all spectral types, ages, and flare energy ranges, we used this more informative, Gaussian prior to further constrain the flaring rates.

Additionally we calculated the exceedance statistic tr to test if the power law distribution was truncated. If tr is 1, the power law distribution is truncated at the high energy end. If tr is 0, no information was gained from the calculation. To derive tr , given a number n of observations X_n and a best fit value for the power law exponent, we generated 500 samples with n values from this best-fit distribution assuming no truncation, i.e. choosing an upper limit several orders of magnitude higher than X_{max} . We then proceeded to truncate the samples at thresholds T below the maximum observed value X_{max} and determined the average number N_{ex} of generated values that will exceed T . If the underlying power law is not truncated, N_{ex} declines with larger n , as larger X_{max} will be present in the original data. If the best fit power law exponent is steeper, N_{ex} will be underestimated. If the best fit power law exponent is flatter, N_{ex} will be overestimated. If the power law is not truncated, for $n \geq 100$ N_{ex}/n will be $< 5\%$, for $20 < n < 100$, typically $N_{ex}/n < 15\%$.

4. Results

Fig. ?? shows the $E_{Kp,\text{flare}}$ and ED detection thresholds, as defined by the recovery probability (see Sec. ??). The thresholds in ED reflect the noise level in the light curves.

⁴ <https://github.com/ekaterinailin/flare-in-clusters-with-k2-ii>

Table 2. Mass budget of flaring stars in M67 and Rup 147 within certainties on radius.

EPIC	median SpT	binary
211434440	K1	K2 + M5.5
219601739	G8	K1 + M6
219610232	K0.5	K2 + M5.5
219591752	M3	M3.5 + M3.5

428 4.1. Flaring activity as a function of age and T_{eff}

429 Flaring activity decays with age. Flaring fraction was observed
 430 to decline with galactic latitude for M dwarfs (Hilton et al.
 431 2010)Howard+2019. Short rotation periods and high magnetic
 432 activity measured in H α are strongly correlated (West et al.
 433 2015). According to gyrochronology, fast rotation indicates
 434 young age (Barnes 2003), and slows down as the star ages. Here
 435 we quantify how this decline unfolds for different spectral types.
 436 Except for the stars in our coolest temperature bin (M5.5-M8
 437 2 500-3 000 K), stellar flaring activity at a given age is always
 438 stronger for a cooler star. The exception is seen at cluster ages
 439 around 120 Myr.
 440 What creates the strong emission in white light? Extended flare
 441 loops, maybe (?)

442 4.2. M67 and Rup 147

443 We found several flare candidates in stars that are members of
 444 M67 and Rup 147. However, all but the events that occurred in
 445 four stars were false positives (SSOs), or the stars were not single
 446 members. Flare candidates in these old clusters appeared on 447
 447 CVn binaries, cataclysmic binaries, Algol type binaries, spectro-
 448 scopic and eclipsing binaries, and red giant stars. Excluding all
 449 these, we were left with one flare in M67 on a K1 dwarf. In Rup
 450 147, we narrowed down the list to a flare on a G8 star in Rup
 451 147, and four flares each on a K0.5 and an M3 star. For the
 452 stars, the multiplicity status is unknown. We found that the mass
 453 range of these stars as calculated from the uncertainties on the
 454 radii (?) is large enough that the stars could in principle be binary
 455 stars with undetected mid-M dwarf companions.

456 4.3. Flaring Activity Indicators

457 Flaring rates: FR and flaring fraction We define FR as the flaring
 458 rate above detection thresholds on $E_{\text{Kp,flare}}$ and ED in each 459
 bin, respectively (Figs. ?? and ??).

507 Flaring energy: FA and $L_{\text{Kp,flare}}$ The energy released in flares
 508 was inferred using our derived stellar luminosities. It declines
 509 with age for every T_{eff} bin considered for both the total luminosity
 510 and relative to the quiescent flux (Fig. ??).

511 $L_{\text{Kp,flare}}$ is the luminosity in flares in the Kepler band. We can relate
 512 this to the quiescent bolometric luminosity of the star when
 513 we define the fractional flare luminosity FA as in Paper I:

$$514 FA = \frac{1}{N} \sum_i^N FA_i = \frac{1}{N} \sum_i^N \frac{E_{\text{Kp,flare,tot},i}}{t_i \cdot L_{\text{bol},*,i}}$$

518 We determine $L_{\text{bol},*}$ from R_* and T_{eff} , as described in Sec. 2.4.
 519 This is a meaningful measure of relative stellar activity as long
 520 as only the flux portion of the quiescent star in the Kepler band is
 521 roughly constant. It is therefore sensible to compare FA values
 522 across ages, but not across T_{eff} .

FFD Power law fit parameters to the FFDs (Figs. ?? and ??)
 466 are sensitive to the low-energy cutoff, where most observations
 467 reside. The goodness of fit strongly depends on the sample size.
 468 Power law fit parameters derived using MLEs, as described in
 469 Sec. 3.3, are mostly consistent with each other but often deviate
 470 from $\alpha = 2$. A smaller sample size tends to create a flatter distribution
 471 (Figs. 7 and ??). Truncation was not detected for FFDs
 472 with more than 50 flares (Tables ?? and ??) For these results, ex-
 473 trapolations outside of the observed energy range are clearly off.
 474 If we assume $\alpha \equiv 2$, different distributions can be compared. For
 475 fixed α , in the ED domain, β_2 is the flare frequency at $ED = 1$ s,
 476 and shows a trend in both T_{eff} , and age (see Fig. ??). In the en-
 477 ergy domain, the picture is less clear (Fig. ??).
 478 Compare to other FFD values, e.g., from Ward's Evryscope sur-
 479 vey, see table in Appendix, and maybe convert it to a plot Howard
 480 et al (2019) monitored superflares on cool stars with bolometric
 481 energies above 10^{33} erg and up to 10^{36} erg. They find power law
 482 exponent values around ~ 2 resolved by spectral types. Similar
 483 values are found for individual flare stars (Lurie et al. 2015).
 484 Howard+18, Loyd+18, Tilley+19 show that flares can erode ex-
 485 oplanetary atmospheres. If a flare is assumed to deposit its UV
 486 energy in an instant a single superflare can completely remove
 487 the ozone layer at the substellar point Loyd+18. Associated pro-
 488 tons are safer way to ozone destruction if they are associated
 489 with reoccurring large flares Tilley+19

5. Discussion

5.1. Consistency with other studies

EvryFlare, mass-dependence,

5.2. Flaring and rotation

More energetic flares can be expected from faster rotating stars (Candelaresi et al. 2014; Doorsselaere et al. 2017; Yang et al. 2017). Findings that flares with intermediate Rossby number appear to flare more than fast and slow rotators (Mondrik et al. 2019) could not be reproduced here or in the EvryFlare survey (Howard et al. 2019b). If enhanced flaring can be interpreted as an increase in the stellar angular momentum loss rate flaring activity can be used to inform the cause of variation in the spin-down efficiency. An example of such variations is the apparent temporary stalling of spin-down seen in K dwarfs in NGC 6811 (Curtis+2019). The authors favored a scenario in which the stellar core transfers momentum onto the envelope but did not rule out the possibility of a decreased magnetic braking efficiency. In the latter scenario, these stars should flare less.

We used rotation periods derived from K2 light curves for the Pleiades (Rebull et al. 2016b), the Hyades (Douglas et al. 2016), and Praesepe (Rebull et al. 2017), to illuminate the rotation-flaring relation at fixed ages. In the Pleiades, most flaring stars are found on the fast rotator branch at or below one day, and flaring activity peaks in this regime. For Praesepe, flaring rates appear t ..[...]. In the Hyades, all of the 11 stars with rotation periods that overlapped with our sample were found flaring, but the number were too low to provide statistical insight. For Rup 147, M35 and M67, no rotation rates were available at the time.

5.3. M37

Comparing our results to a similar study of photometric flares in M37 (Chang et al. 2015) we find the results somewhat discrepant. M37 is 300-600 Myr old and appears less active than

Table 3. Summary of flaring β of all clusters and T_{eff} bins in energy and ED distributions.

			β_s	n_s	tr_s	pl_s	β_{erg}	n_{erg}	tr_{erg}	pl_{erg}
2500-3000	Hyades	2.67	$(0.1) \cdot 10^3$	27	False	True	$0.53 (0.02) \cdot 10^{28}$	27	False	True
		Pleiades	$0.86 (0.04) \cdot 10^3$	23	False	True	$1.96 (0.08) \cdot 10^{27}$	23	False	True
		Praesepe	$0.784 (0.025) \cdot 10^3$	5	False	True	$2.264 (0.07) \cdot 10^{27}$	5	False	True
3000-3250	Hyades	1.36	$(0.04) \cdot 10^3$	133	False	True	$1.134 (0.031) \cdot 10^{28}$	133	False	True
		Pleiades	$1.925 (0.059) \cdot 10^3$	623	False	True	$1.253 (0.034) \cdot 10^{28}$	623	True	True
		Praesepe	$1.224 (0.038) \cdot 10^3$	289	True	True	$1.025 (0.028) \cdot 10^{28}$	289	True	True
3250-3500	Hyades	1.046	$(0.032) \cdot 10^3$	175	True	True	$2.308 (0.063) \cdot 10^{28}$	175	False	True
		Pleiades	$1.713 (0.052) \cdot 10^3$	597	True	True	$3.103 (0.085) \cdot 10^{28}$	597	True	True
		Praesepe	$1.054 (0.032) \cdot 10^3$	477	True	True	$2.052 (0.056) \cdot 10^{28}$	477	True	False
3500-3750	Hyades	1.71	$(0.16) \cdot 10^2$	4	False	True	$0.35 (0.03) \cdot 10^{28}$	4	False	True
		Pleiades	$0.87 (0.03) \cdot 10^3$	49	False	True	$0.5 (0.02) \cdot 10^{29}$	49	False	True
		Praesepe	$2.18 (0.08) \cdot 10^2$	54	False	True	$1.248 (0.037) \cdot 10^{28}$	54	False	True
3750-4000	Pleiades	0.6	$(0.02) \cdot 10^3$	78	False	True	$0.77 (0.03) \cdot 10^{29}$	78	False	False
		Praesepe	$0.74 (0.17) \cdot 10^2$	15	False	True	$0.94 (0.03) \cdot 10^{28}$	15	False	True
		Hyades	$1.96 (0.2) \cdot 10^1$	12	False	True	$0.73 (0.07) \cdot 10^{28}$	12	False	True
4000-5000	Pleiades	0.471	$(0.015) \cdot 10^3$	131	False	True	$1.238 (0.034) \cdot 10^{29}$	131	False	True
		Praesepe	$2.64 (0.12) \cdot 10^1$	26	False	True	$1.13 (0.04) \cdot 10^{28}$	26	False	True
		M67	$0.61 (0.03) \cdot 10^1$	1	True	False	$0.56736 (3e-05) \cdot 10^{..}$	1	True	False
5000-6000	Pleiades	0.64	$(0.06) \cdot 10^2$	36	False	True	$0.67 (0.04) \cdot 10^{29}$	36	False	True
		Praesepe	$2.65 (0.09) \cdot 10^1$	36	False	True	$2.82 (0.1) \cdot 10^{28}$	36	False	True
		Rup 147	$0.54 (0.13) \cdot 10^2$	5	False	True	$0.44 (0.07) \cdot 10^{29}$	5	False	True

522 Praesepe and Hyades in individual Teff bins, which are of coesee
 523 or older. We attribute the difference to the loose membership 557
 524 requirement of $pmem \geq 0.2$ in Chang et al. (2015) as compared 558
 525 to our stricter cuts at 0.8. We expect the M37 to be contaminated 559
 526 with field stars that systematically reduce the flaring rates. Appling 560
 527 our own restriction the M37 sample (Chang et al. 2016) leaves very few flares that hamper a statistical description of their 529 distributions.

Assuming a typical binary fraction for early and mid M dwarfs (Fischer & Marcy 1992), we can expect some of the flares on stars at $T_{\text{eff}} > 3000$ K to belong to unresolved binary companions with $T_{\text{eff}} < 3000$ K. A misattributed flare on an early M dwarf then will be assigned a too small ED , but still a correct $E_{Kp,\text{flare}}$ because the count ratios are equal to the L_{Kp} ratios.

5.4. Division at 3000 K

531 The lowest T_{eff} bin at Pleiades age in our sample reflects 545 division between fully convective stars and those with a radiative 546 core (Reid & Hawley 2005). At this age, the coolest dwarfs 547 may still be accreting angular momentum on the PMS, instead 548 of spinning down on the MS. We suggest that a regime change 549 occurs around 120 Myr for stars with $T_{\text{eff}} = 2500 - 3250$ K. 550 Below 3000 K, an analysis of 66 ZDI maps show that magnetic 551 field configurations can be strong and dipolar or weak and 552 tipolar (Morin et al. 2008; See et al. 2017). If these stars can be 553 distinguished by age, this should be reflected in our age-resolved 554 flaring activity. If the difference is not a function of age, we 555 should see a similar bimodal distribution of very inactive and 556 very active stars in the lowest mass bins. If the difference between 557 the two configurations is a function of age, we should only 558 see one type of stars with correspondingly similar behaviour in 559 these T_{eff} bins.

560 The lowest mass bin appears underactive compared to the rest 561 of the flaring-age- T_{eff} relation in the ED domain. Physical explanations 562 for this peculiarity include: A different magnetic structure 563 A truncation of the power law that reflects the maximum ED 564 active region can produce on these stars. 565 West et al. (2015) found that all M1-M4 dwarfs with rotation 566 periods shorter than 26 days, and all M5-M8 dwarfs with periods 567 shorter than 86 days show H α emission, indicating their magnetic 568 activity. 569

5.5. Consistency of Hyades' and Praesepe's results

562 HRDs constructed in Gaia Collaboration et al. (2018a) indicate 563 only slightly older ages for Hyades and Praesepe. We expect our 564 results to reflect this similarity.

Are the samples comparable? Membership determination may differ. Can we frame this as a statistical test, i.e. answer the question: What is the probability that the activity distributions for both clusters were drawn from the same underlying distribution for a given age and mass bin?

565 Metallicity is controlled for ([Fe/H](Praesepe) = 0.16, [Fe/H](Hyades) = 0.13, Netopil et al. 2016).

5.6. Consistency of Pleiades and M35 results

566 M35 is has subsolar metallicity, while Pleiades are roughly solar.

5.7. Jim's section(s)

Flaring activity function of mass and age – a gyrochronology analog?

Results in the context of Davenport et al. (2019): How well does the model fit if we have isochronal and not rotational ages for our stars?

Davenport et al. (2019) note a sample bias towards more active stars. Their models overpredicts the superflaring rate of the average Sun-like sample from Shibayama et al. (2013) and more resembles the rate for their most active sub-sample. Do we see

585 the same effect in our OC sample? We should not. Or cluster
 586 memberships depend on activity.

587 5.8. Universality of α

588 Takin into account uncertainties and systematic errors resulting
 589 power law fitting methods, the power law exponent $\alpha \sim 2$
 590 pears to be the same for all studies on flare statistics so far, if
 591 respective of spectral type. A noteable exception are A stars
 592 Kepler that follow a power law with $\alpha \sim 1$ that may indicate
 593 different physical process (Yang & Liu 2019).

594 5.9. Deviations from single power law

595 Spots can survive on the stellar surface from a few days to nearly
 596 a year (Namekata et al. 2017; Davenport 2015). Namekata et al.
 597 (2017) find conceivable that spots evolve on timescale shorter
 598 than the estimated lifetimes. Complex spot geometry is corre-
 599 lated with the strongest X-class flares on the Sun (Toriumi et al.
 600 2017; Sammis et al. 2000). This support the idea that flares are
 601 associated with the presence of certain types of starspots, or
 602 more generally, certain types of active regions. Since we can rea-
 603 sonable expect that there is a maximum flare energy a spot can
 604 produce, the underlying power law relation must break a so-called
 605 ED_{\max} . We tested a possible truncation of our FFDs, but find
 606 conclusive evidence for it in any FFD with > 50 data points. If
 607 we stack multiple targets, each potentially with multiple, evolv-
 608 ing spots of various sizes on their surfaces, into one FFD at a
 609 time, we might observe a deviation but no truncation. A differ-
 610 ent explanation is simply that we do not sample the maximum
 611 energies, as extremely high relative fluxes have been observed in
 612 the past (Paudel et al. 2018; Jackman et al. 2019; Schmidt et al.
 613 2016).

614 6. Summary and Conclusions

615 Is there or will be there more data available to further extend
 616 sample? There are no model-independent stellar ages. It is more
 617 correct to speak of evolutionary stage. Stars in open clusters with
 618 precise isochronal ages have their observables reduced to a num-
 619 ber of years. We can now ask: Can we unambiguously map flares
 620 ing evolutionary stage to the evolutionary stage of isochronal
 621 parameters of a given star? If there is either a strong correlation
 622 or even a physical relation between flaring activity and, for in-
 623 stance, mass and rotation rate, the answer is yes. If this relation
 624 is sufficiently sensitive to be captured by present day instrumen-
 625 tation, and non-degenerate in the relevant parameters, flaring
 626 activity can be integrated into the family of age indicators, and
 627 complement and extend them.

628 Ultimately, flaring activity depends on how efficiently the star
 629 converts its energy budget to flares throughout its lifetime. Since
 630 the fraction of total luminosity released in flares is small even
 631 for the most active stars, this efficiency need not scale directly
 632 with the overall energy budget of the star on the MS, but will
 633 more likely depend on the ability of the star to use this budget
 634 to produce magnetic surface topologies and strengths that enable
 635 flaring.

636 A magnetic dynamo, driven by rotation and convection, intro-
 637 duces magnetic field to the system that causes stellar wind that
 638 in turn removes angular momentum from the star, decreasing
 639 rotation rate. Over time, the wind takes away more and more an-
 640 gular momentum, and the global magnetic field weakens. This is
 641 reflected in observations of chromospheric indicators (ZDI???)

The decline is famously known as the Skumanich law, and gave rise to the rotational age-dating technique called gyrochronology. However, recent studies noted deviations from this rule, a stalling of the spin-down, and offered multiple competing explanations. It is not clear how these effects reflect on the small scale surface magnetic field. Chromospheric activity on solar type stars seems to continue to decline regardless of these rotational effects.

What about X-ray?

Observationally, not much can be directly said about the small scale topology of stellar magnetic fields beyond extrapolations from the solar case. On the Sun, chromospheric activity indicates line emission in excess of radiative equilibrium that is caused by magnetic fields. Likewise, magnetic field effects heat the corona

Acknowledgements. This work made use of the `gaia-kepler.fun` crossmatch database created by Megan Bedell. Kepler-affiliated tools were used in the process: `lightkurve`, `K2SC`, `AltaIPony`. Also: `numpy`, `pandas`, `astroML`, `astropy`, `specmatch-emp`, `bokeh` (Bokeh Development Team 2019)... `TOPCAT`: This research made use of the cross-match service provided by CDS, Strasbourg. This work has made use of data from the European Space Agency (ESA) mission `Gaia` (<https://www.cosmos.esa.int/gaia>), processed by the `Gaia` Data Processing and Analysis Consortium (DPAC, <https://www.cosmos.esa.int/web/gaia/dpac/consortium>). Funding for the DPAC has been provided by national institutions, in particular the institutions participating in the `Gaia` Multilateral Agreement. If you have used `Gaia` DR2 data in your research, please cite both the `Gaia` mission paper and the `Gaia` DR2 release paper: `Gaia` Collaboration et al. (2016): Description of the `Gaia` mission (spacecraft, instruments, survey and measurement principles, and operations), `Gaia` Collaboration et al. (2018b): Summary of the contents and survey properties.

References

- Aarnio, A. N., Matt, S. P., & Stassun, K. G. 2012, *ApJ*, 760, 9
- Aarnio, A. N., Stassun, K. G., Hughes, W. J., & McGregor, S. L. 2011, *Sol. Phys.*, 268, 195
- Aigrain, S., Parviainen, H., & Pope, B. J. S. 2016, *MNRAS*, 459, 2408
- Alvarado-Gómez, J. D., Drake, J. J., Cohen, O., Moschou, S. P., & Garraffo, C. 2018, *ApJ*, 862, 93
- Anders, F., Khalatyan, A., Chiappini, C., et al. 2019, *A&A*, 628, A94
- Andrae, R., Fouesneau, M., Creevey, O., et al. 2018, *A&A*, 616, A8
- Bailer-Jones, C. A. L., Andrae, R., Arcay, B., et al. 2013, *A&A*, 559, A74
- Barentsen, G., Hedges, C., Saunders, N., et al. 2018, arXiv e-prints, arXiv:1810.12554
- Barnes, S. A. 2003, *ApJ*, 586, 464
- Bauke, H. 2007, *European Physical Journal B*, 58, 167
- Bessell, M. S. & Brett, J. M. 1988, *Publications of the Astronomical Society of the Pacific*, 100, 1134
- Bochanski, J. J., Hawley, S. L., Covey, K. R., et al. 2010, *AJ*, 139, 2679
- Bochanski, J. J., West, A. A., Hawley, S. L., & Covey, K. R. 2007, *AJ*, 133, 531
- Bokeh Development Team. 2019, Bokeh: Python library for interactive visualization
- Bouy, H., Bertin, E., Barrado, D., et al. 2015, *Astronomy and Astrophysics*, 575, A120
- Boyajian, T. S., von Braun, K., van Belle, G., et al. 2013, *The Astrophysical Journal*, 771, 40
- Burgasser, A. J., Cruz, K. L., Cushing, M., et al. 2010, *ApJ*, 710, 1142
- Burgasser, A. J., Liu, M. C., Ireland, M. J., Cruz, K. L., & Dupuy, T. J. 2008, *ApJ*, 681, 579
- Burgasser, A. J.,Looper, D. L., Kirkpatrick, J. D., & Liu, M. C. 2007, *ApJ*, 658, 557
- Burgasser, A. J. & McElwain, M. W. 2006, *AJ*, 131, 1007
- Burgasser, A. J., McElwain, M. W., Kirkpatrick, J. D., et al. 2004, *AJ*, 127, 2856
- Candelaresi, S., Hillier, A., Maehara, H., Brandenburg, A., & Shibata, K. 2014, *ApJ*, 792, 67
- Cantat-Gaudin, T., Jordi, C., Vallenari, A., et al. 2018, *A&A*, 618, A93
- Carpenter, J. M. 2001, *The Astronomical Journal*, 121, 2851
- Chambers, K. C., Magnier, E. A., Metcalfe, N., et al. 2016, ArXiv e-prints [arXiv: 1612.05560]
- Chang, S.-W., Byun, Y.-I., & Hartman, J. D. 2015, *ApJ*, 814, 35
- Chang, S. W., Byun, Y. I., & Hartman, J. D. 2016, *VizieR Online Data Catalog*, J/ApJ/814/35
- Clarke, R. W., Davenport, J. R. A., Covey, K. R., & Baranec, C. 2018, *ApJ*, 853, 59

- 713 Cruz, K. L., Burgasser, A. J., Reid, I. N., & Liebert, J. 2004, ApJ, 604, L61 792
 714 Cruz, K. L., Reid, I. N., Liebert, J., Kirkpatrick, J. D., & Lowrance, P. J. 20793
 715 AJ, 126, 2421 794
 716 Curtis, J. L., Wolfgang, A., Wright, J. T., Brewer, J. M., & Johnson, J. A. 20795
 717 AJ, 145, 134 796
 718 Davenport, J. 2015, PhD thesis, University of Washington 797
 719 Davenport, J. R. A., Covey, K. R., Clarke, R. W., et al. 2019, ApJ, 871, 241 798
 720 Davenport, J. R. A., Hawley, S. L., Hebb, L., et al. 2014, ApJ, 797, 122 799
 721 Doi, M., Tanaka, M., Fukugita, M., et al. 2010, AJ, 139, 1628 800
 722 Doorsselaere, T. V., Shariati, H., & Debosscher, J. 2017, ApJS, 232, 26 801
 723 Douglas, S. T., Agüeros, M. A., Covey, K. R., et al. 2014, ApJ, 795, 161 802
 724 Douglas, S. T., Agüeros, M. A., Covey, K. R., et al. 2016, ApJ, 822, 47 803
 725 Douglas, S. T., Agüeros, M. A., Covey, K. R., & Kraus, A. 2017, ApJ, 842, 804
 726 Drake, J. J., Cohen, O., Yashiro, S., & Gopalswamy, N. 2013, ApJ, 764, 170805
 727 Filippazzo, J. C., Rice, E. L., Faherty, J., et al. 2015, ApJ, 810, 158 806
 728 Finkbeiner, D. P., Schlafly, E. F., Schlegel, D. J., et al. 2016, ApJ, 822, 66 807
 729 Fischer, D. A. & Marcy, G. W. 1992, ApJ, 396, 178 808
 730 Froning, C. S., Kowalski, A., France, K., et al. 2019, ApJ, 871, L26 809
 731 Gaia Collaboration, Babusiaux, C., van Leeuwen, F., et al. 2018a, A&A, 616 810
 732 A10 811
 733 Gaia Collaboration, Brown, A. G. A., Vallenari, A., et al. 2018b, A&A, 616, 812
 734 Gao, X. 2018, ApJ, 869, 9 813
 735 Gao, X. 2018, The Astrophysical Journal, 869, 9 814
 736 Gizis, J. E. 2013, ApJ, 779, 172 815
 737 Gonzalez, G. 2016, MNRAS, 459, 1060 816
 738 Green, G. M., Schlafly, E. F., Finkbeiner, D., et al. 2018, MNRAS, 478, 651 817
 739 Green, G. M., Schlafly, E. F., Zucker, C., Speagle, J. S., & Finkbeiner, D. 818
 740 2019, arXiv e-prints, arXiv:1905.02734 819
 741 Hawley, S. L. & Fisher, G. H. 1992, ApJS, 78, 565 820
 742 Hilton, E. J., West, A. A., Hawley, S. L., & Kowalski, A. F. 2010, AJ, 140, 1402 821
 743 Howard, W. S., Corbett, H., Law, N. M., et al. 2019a, ApJ, 881, 9 822
 744 Howard, W. S., Corbett, H., Law, N. M., et al. 2019b, arXiv e-prints 823
 745 arXiv:1907.10735 824
 746 Howell, S. B., Sobeck, C., Haas, M., et al. 2014, PASP, 126, 398 825
 747 Hunt-Walker, N. M., Hilton, E. J., Kowalski, A. F., Hawley, S. L., & Matthews, J. M. 2012, PASP, 124, 545 826
 748 Ilin, E., Schmidt, S. J., Davenport, J. R. A., & Strassmeier, K. G. 2019, A&A, 622, A133
 749 Jackman, J. A. G., Wheatley, P. J., Bayliss, D., et al. 2019, arXiv e-prints, 750 arXiv:1902.00900
 751 Karoff, C. 2016, Nature Communications, 7, 11058
 752 Kerr, G. S. & Fletcher, L. 2014, ApJ, 783, 98
 753 Kirkpatrick, J. D.,Looper, D. L.,Burgasser, A. J.,et al. 2010, ApJS, 190, 100
 754 Kleint, L.,Heinzel, P.,Judge, P.,&Krucker, S. 2016, ApJ, 816, 88
 755 Koch, D. G., Borucki, W. J., Basri, G., et al. 2010, ApJ, 713, L79
 756 Kovács, G., Bakos, G., & Noyes, R. W. 2005, MNRAS, 356, 557
 757 Kowalski, A. F., Hawley, S. L., Wisniewski, J. P., et al. 2013, ApJS, 207, 15
 758 Kretzschmar, M. 2011, A&A, 530, A84
 759 Lecavelier des Etangs, A., Bourrier, V., Wheatley, P. J., et al. 2012, A&A, 543, 760 L4
 761 Loyd, R. O. P., France, K., Youngblood, A., et al. 2018, ApJ, 867, 71
 762 Luger, R., Kruse, E., Foreman-Mackey, D., Agol, E., & Saunders, N. 2018, AJ, 763 156, 99
 764 Lurie, J. C., Davenport, J. R. A., Hawley, S. L., et al. 2015, ApJ, 800, 95
 765 Mann, A. W., Feiden, G. A., Gaidos, E., Boyajian, T., & von Braun, K. 2015, 766 ApJ, 804, 64
 767 Mann, A. W., Feiden, G. A., Gaidos, E., Boyajian, T., & von Braun, K. 2016, 768 The Astrophysical Journal, 819, 87
 769 Maschberger, T. & Kroupa, P. 2009, MNRAS, 395, 931
 770 Mondrik, N., Newton, E., Charbonneau, D., & Irwin, J. 2019, ApJ, 870, 10
 771 Morin, J., Donati, J. F., Petit, P., et al. 2008, MNRAS, 390, 567
 772 Namekata, K., Sakaue, T., Watanabe, K., et al. 2017, ApJ, 851, 91
 773 Nardiello, D., Libralato, M., Bedin, L. R., et al. 2016, MNRAS, 463, 1831
 774 Olivares, J., Bouy, H., Sarro, L. M., et al. 2019, A&A, 625, A115
 775 Olivares, J., Sarro, L. M., Moraux, E., et al. 2018, A&A, 617, A15
 776 Paudel, R. R., Gizis, J. E., Mullan, D. J., et al. 2018, ApJ, 861, 76
 777 Pecaut, M. J. & Mamajek, E. E. 2013, ApJS, 208, 9
 778 Priest, E. & Forbes, T. 2002, A&A Rev., 10, 313
 779 Queiroz, A. B. A., Anders, F., Santiago, B. X., et al. 2018, MNRAS, 476, 2556
 780 Rayner, J. T., Cushing, M. C., & Vacca, W. D. 2009, ApJS, 185, 289
 781 Rebull, L., Stauffer, J., Bouvier, J., et al. 2016a, Astronomical Journal, 152, 113, 782 bibcode: 2016AJ....152..113R
 783 by the SAO/NASA Astrophysics Data System
 784 Rebull, L. M., Stauffer, J. R., Bouvier, J., et al. 2016b, AJ, 152, 113
 785 Rebull, L. M., Stauffer, J. R., Hillenbrand, L. A., et al. 2017, ApJ, 839, 92
 786 Reid, I. N. & Hawley, S. L. 2005, New Light on Dark Stars: Red Dwarfs, Low-
 787 Mass Stars, Brown Dwarfs, 2nd edn., Springer-Praxis books in astronomy and
 788 astrophysics (Berlin ; New York : Chichester, UK: Springer ; Praxis

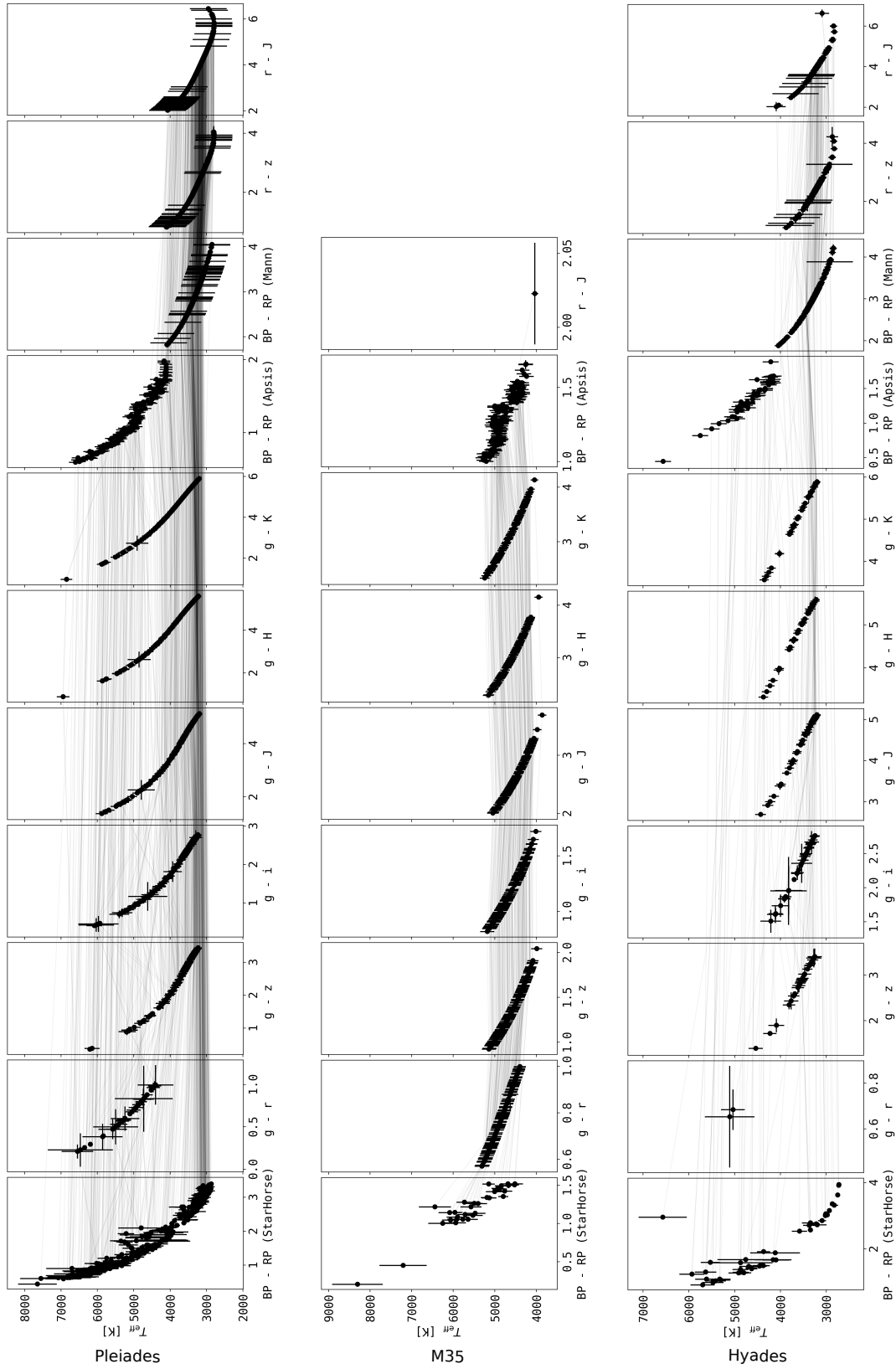


Fig. 2. Color-temperature relations for Pleiades, M35, and Hyades.

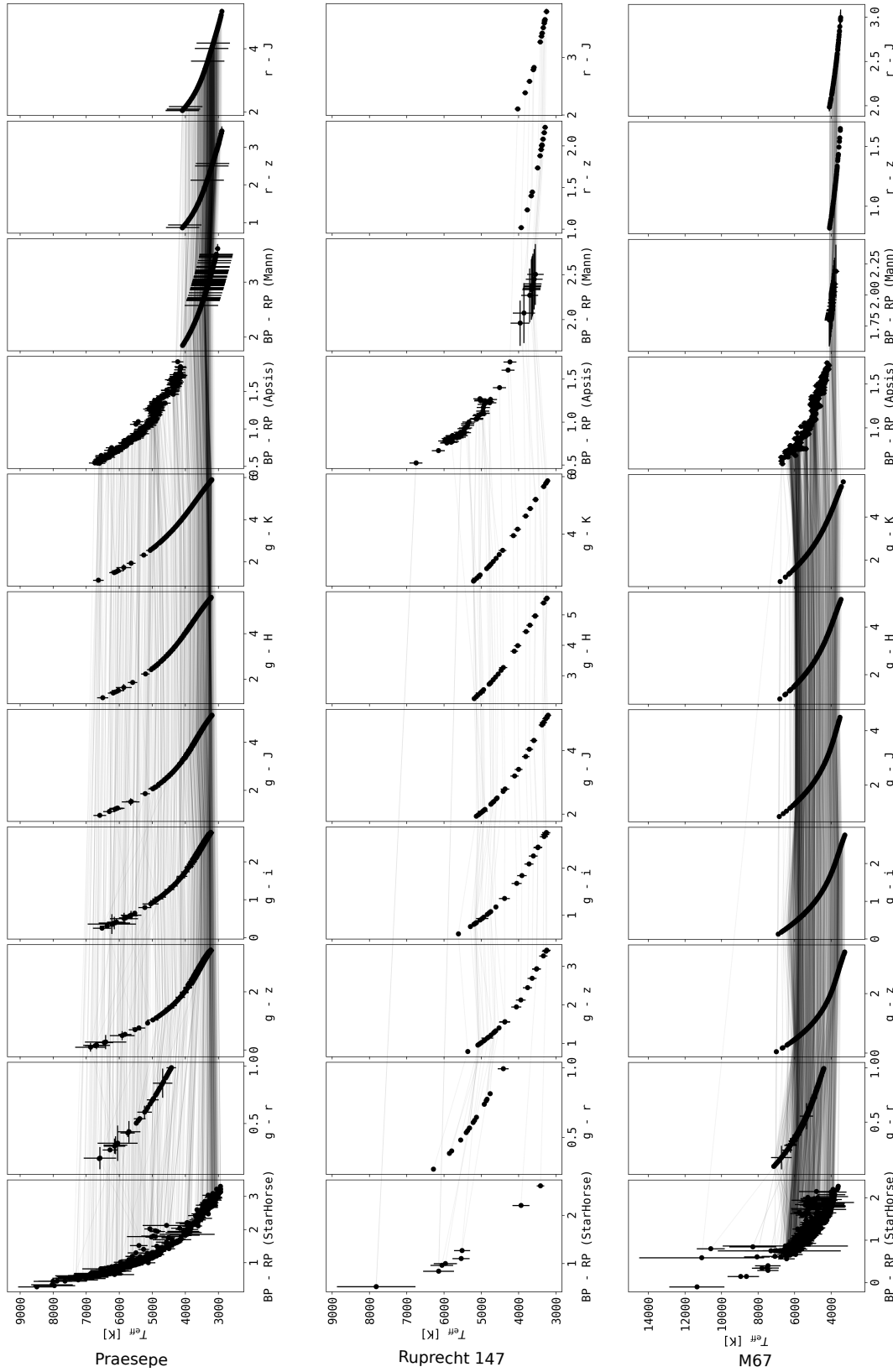
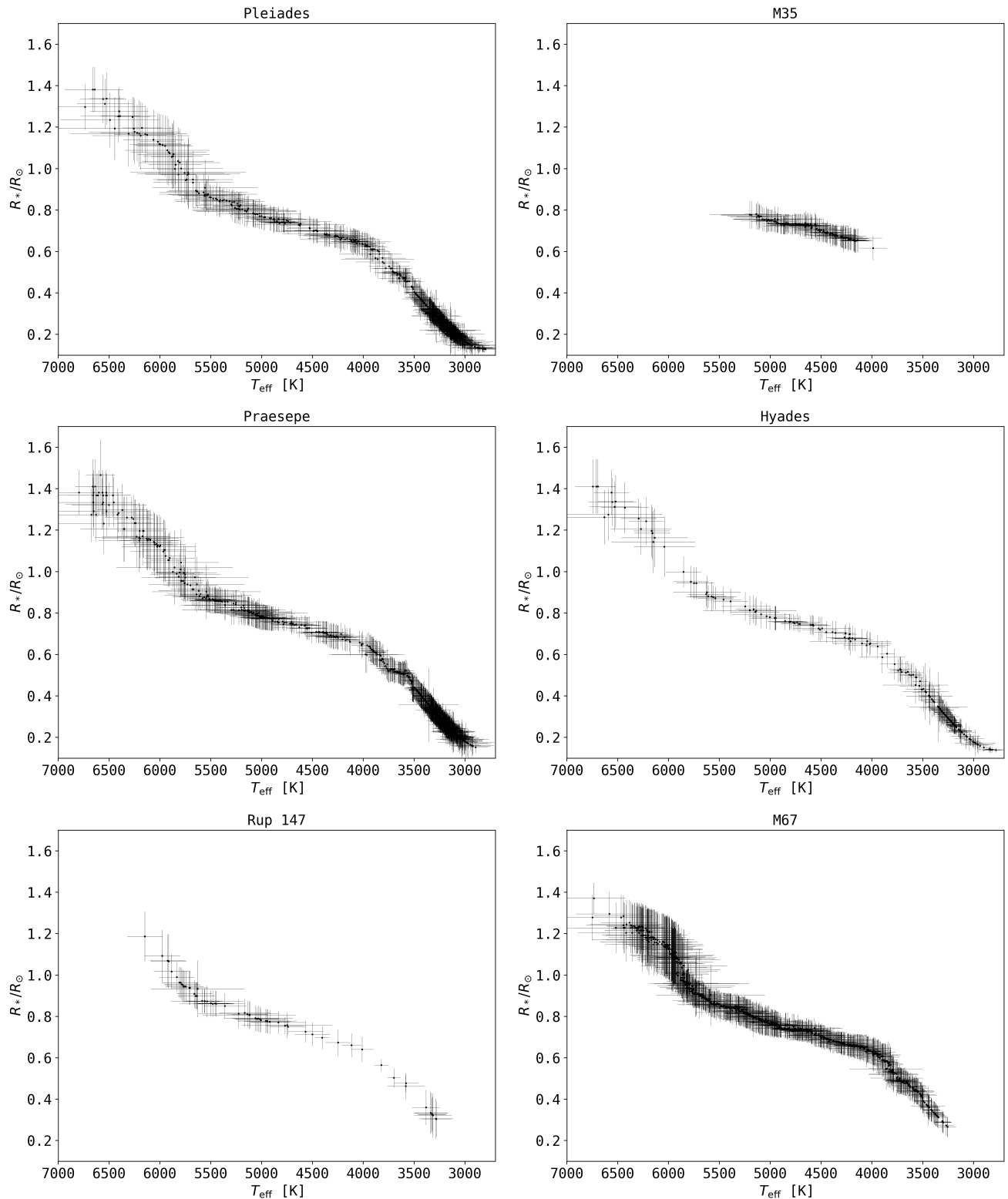


Fig. 3. Color-temperature relations for Praesepe, Ruprecht 147, and M67. Description as in Fig. 2.

**Fig. 4.** $T_{\text{eff}} - R_*$ relation for all clusters in this study.

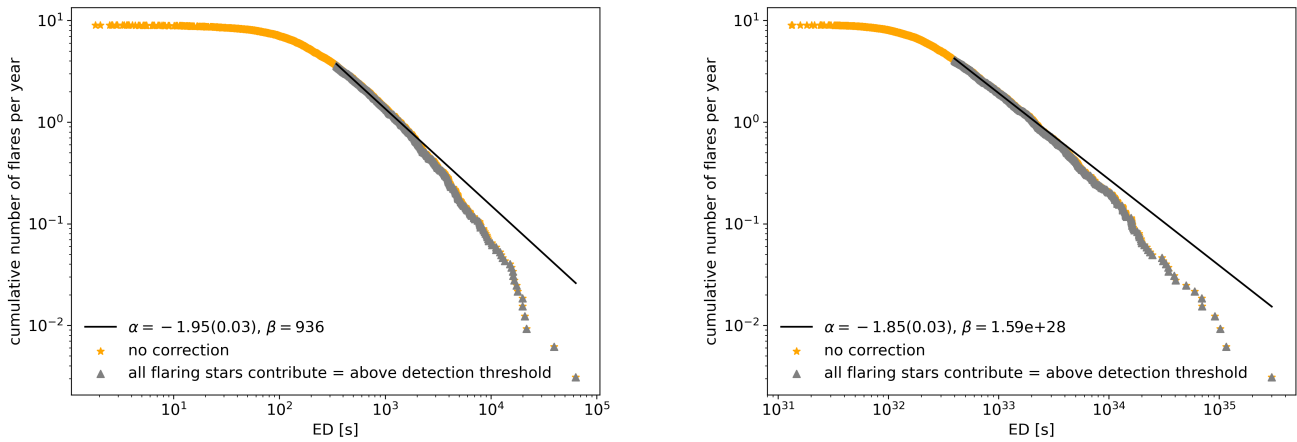


Fig. 5. FFD (scatter) in ED (left panel) and energy (right panel) and respective power law fit (black line) to the full sample of flare candidates.

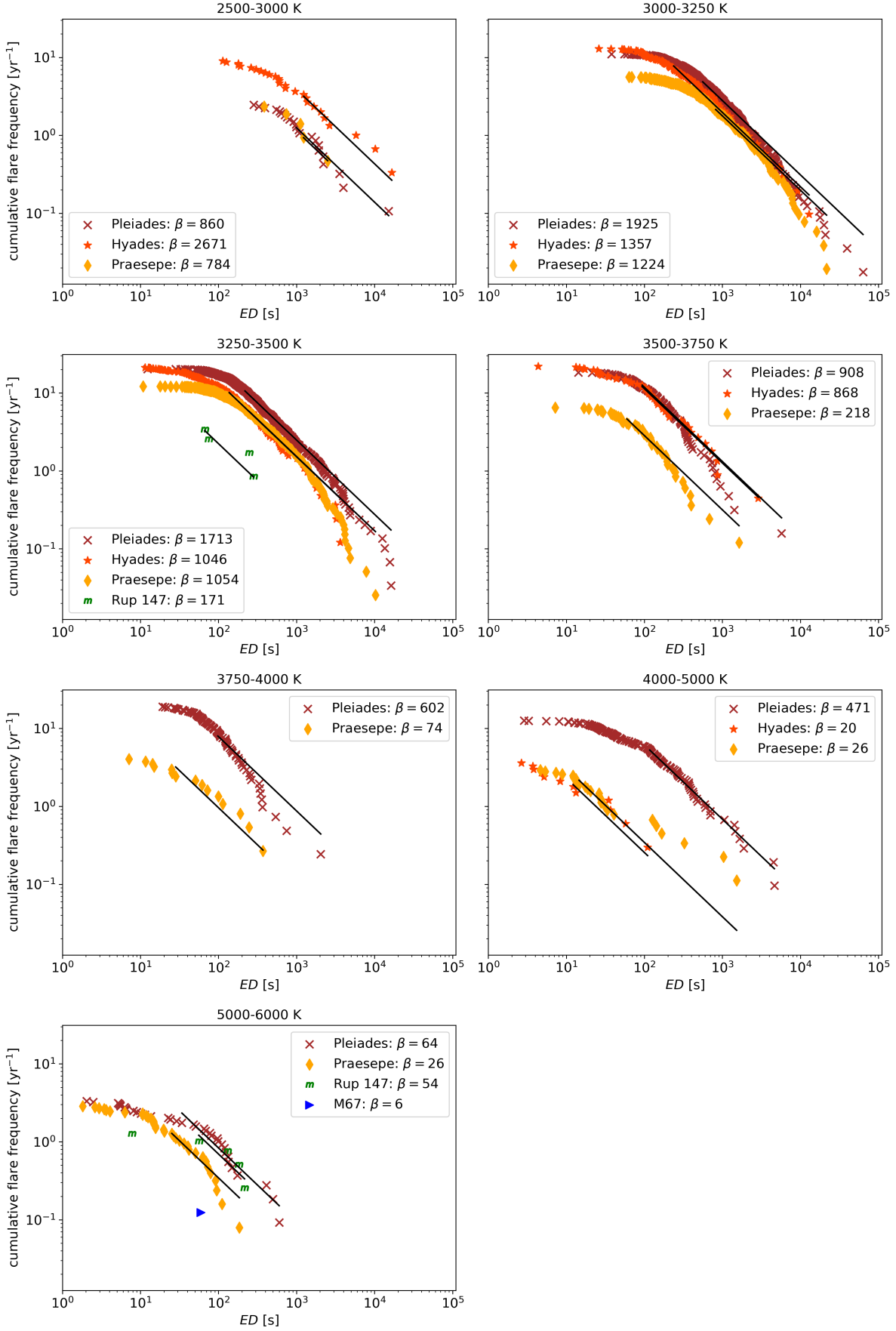


Fig. 6. FFDs (scatter) in ED and respective power law fits with $\alpha = XXX$ (black lines).

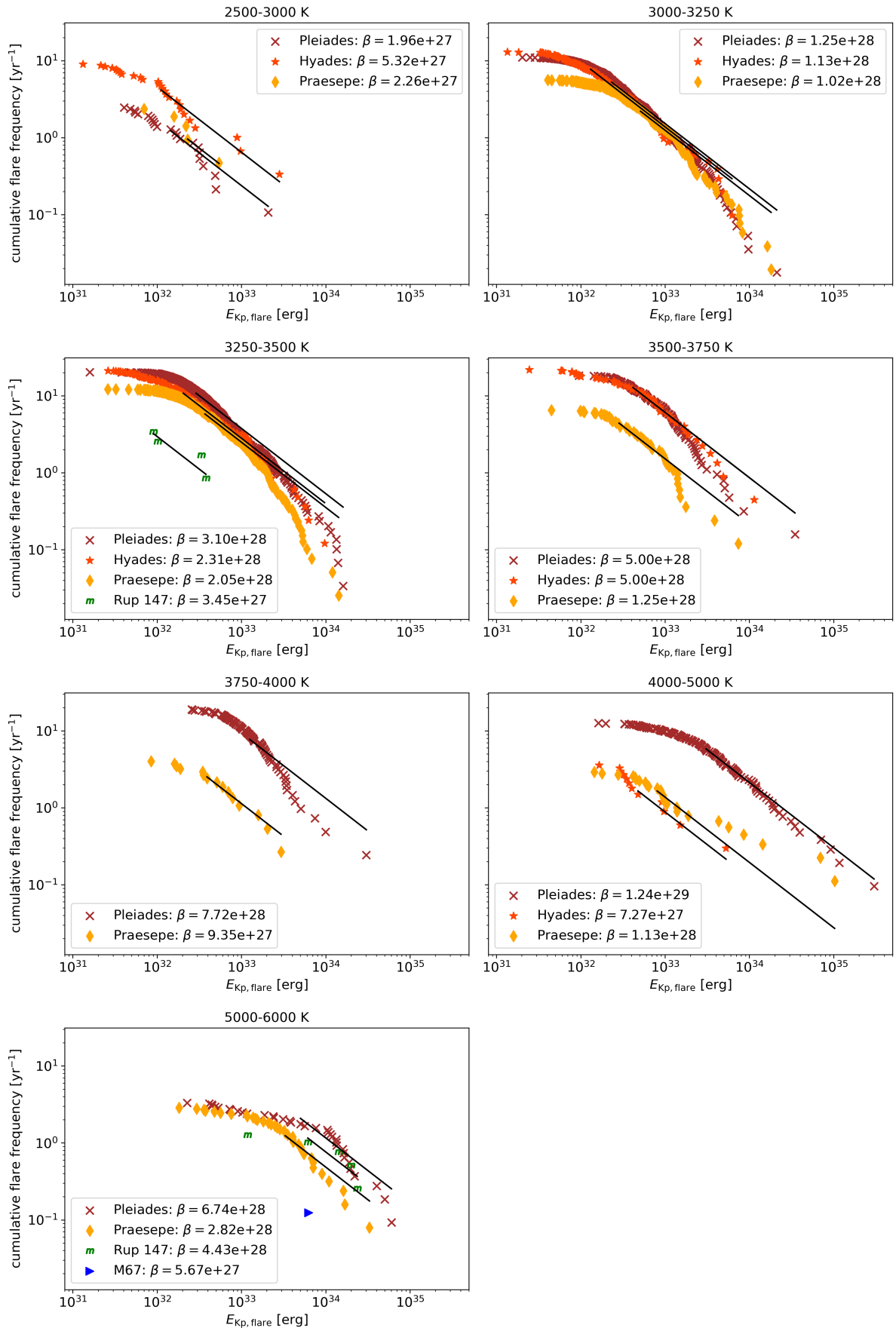


Fig. 7. FFDs (scatter) in energy and respective power law fits with $\alpha = XXX$ (black lines).

827 Appendix A: Membership probabilities

828 To match catalogs on RA and declination we used `astroML.crossmatch` tool for Python (Vanderplas et al. 2012)
 829 For the studies with classifiers we assigned membership proba
 830 bilities as follows. In Gonzalez (2016):
 831

$$\begin{aligned} p(M(\text{member})) &= 0.9, \\ p(BM(\text{binary member})) &= 0.9, \\ p(N(\text{non-member})) &= 0.1, \\ p(SN(\text{single non-member})) &= 0.1, \\ p(BN(\text{binary non-member})) &= 0.1, \\ p(U(\text{unknown member})) &= 0.5. \end{aligned}$$

832 In Curtis et al. (2013):

$$\begin{aligned} p(Y(\text{highest confidence member})) &= 0.9, \\ p(P(\text{possible/probable member})) &= 0.7, \\ p(N(\text{not likely/non-member})) &= 0.7, \\ p(B(\text{photometry consistent with blue stragglers})) &= 0.0. \end{aligned}$$

833 In Rebull et al. (2017):

$$\begin{aligned} p((\text{best})) &= 0.9, \\ p((\text{ok})) &= 0.6, \\ p((\text{else})) &= 0.1. \end{aligned}$$

834 Members from Rebull et al. (2016a); Douglas et al. (2017); and
 835 Gaia Collaboration et al. (2018a) were assigned $p = 0.9$ if they
 836 appeared in the final catalog.
 837 Table A.1 gives an overview over different membership catalogues.
 838 Figure A.1 shows membership probability histograms of the final sample broken down by membership source. Detailed instructions on how to reproduce the final sample of members in each cluster, and corresponding tables, Python scripts, and Jupyter notebooks can be found online⁵

843 Appendix B: Cluster parameters

844 Appendix C: Broadband photometry: quality cuts 845 and conversions

846 We required `flux/flux_error` ≥ 10 for Gaia G, BP, and RP
 847 bands. We require that the 2MASS measurements for J, H, and
 848 K to be "A". "A" means that measurements had $S/N > 10$ and
 849 $\sigma < 0.11$. For PanSTARRS photometry, we required that the
 850 QF_OBJ_GOOD quality filter flag was set.
 851 SDSS and PS1 *ugrizy* bands are similar but not identical, but can
 852 be converted using Table 2 in Finkbeiner et al. (2016).

853 Appendix D: Pixel saturation

854 Resolve different levels of pixel saturation (>1 , >10) and how
 855 they contribute to the deviations from the single power law at
 856 the highest energies.

⁵ <https://github.com/ekaterinailin/flares-in-clusters-with-k2-ii>

857 Appendix E: Solar system objects

858 Solar system objects (SSOs) produce brightness excursions in
 859 K2 light curves that can closely resemble flare signatures. Often,
 860 they can be distinguished by their symmetric rise and decay
 861 shape as contrasted with the typical fast-rise gradual decay flare
 862 shape (Davenport et al. 2014). M. H. Christiansen and colleagues
 863 developed a routine called SkyBoT that matches positions and
 864 times to passages of SSOs listed in YYY. RA, declination, start,
 865 stop, and mid epochs of flares in BKJD are the input parameters.
 866 We excluded all flare candidates that occurred within X minutes
 867 of a SSO passage at the star's position. This procedure removed
 868 ZZ% of all flare candidates. In the case of high energy flares, we
 869 confirmed the passage by manually inspecting the pixel file with
 870 the `lightkurve interact` function for TargetPixelFiles.

871 Appendix F: Universality of power law exponent α

872 We compiled a exhaustive (?) table of previous work where
 873 power laws were fitted to FFDs using different methods. Table
 874 F.1 lists the overview. While particular studies consistently find
 875 values above or below $\alpha \approx 2$, the comparison of different studies
 876 points towards unresolved systematic errors in all these studies.

877 Appendix G: Expanding the likelihood

The rate λ_2 of flares with energies larger than S_2 is given in Wheatland (2004) as

$$\lambda_2 = \lambda_1 \cdot \left(\frac{S_1}{S_2} \right)^{\alpha-1}. \quad (\text{G.1})$$

S_1 denotes the energy above which all flares are detected. λ_1 is the corresponding rate. α remains the power law exponent of the flare frequency distribution.

We are also given the posterior distribution for the rate λ_2 of flares above S_2 in Eq. (20) in Wheatland (2004):

$$\begin{aligned} P_2(\lambda_2) &= \int_1^\infty d\alpha \int_0^\infty d\lambda_1 \delta\left(\lambda_2 - \lambda_1 \cdot \left(\frac{S_1}{S_2} \right)^{\alpha-1}\right) \\ &\quad \cdot P_1(\lambda_1) \cdot P_\alpha(\alpha) \end{aligned} \quad (\text{G.2})$$

As we have additional information in the form of uncertainties in our data $S = \{S_i, \lambda_i, \sigma_{S,i}\}$, we can expand Eq. G.2 with this knowledge. Assuming that the observed flare energies S_i with cumulative rates λ_i are distributed around the real flare energies $S_{0,i}$ with Gaussian uncertainties $\sigma_{S,i}$, we can define:

$$\begin{aligned} p(S_i|\lambda_1, \alpha, \sigma_{S,i}) &= \frac{1}{2\pi\sqrt{\sigma_{S,i}}} e^{-\frac{(S_i - S_{0,i})^2}{2\sigma_{S,i}^2}} \\ &\quad - \frac{\left(S_i - S_1 \left(\frac{\lambda_i}{\lambda_1} \right)^{-1/(\alpha-1)} \right)^2}{2\sigma_{S,i}^2} \end{aligned} \quad (\text{G.3})$$

We assume in Eq. G.3 that uncertainties on λ_1 are negligible. Eq. G.2 then reads:

$$\begin{aligned} P_2(\lambda_2) &= \int_1^\infty d\alpha \int_0^\infty d\lambda_1 \delta\left(\lambda_2 - \lambda_1 \cdot \left(\frac{S_1}{S_2} \right)^{\alpha-1}\right) \\ &\quad \cdot P_1(\lambda_1) \cdot P_\alpha(\alpha) \cdot P_S(S|\lambda_1, \alpha, \sigma_S) \end{aligned} \quad (\text{G.4})$$

Table A.1. Membership catalogs overview. No distance are given for Hyades we adopted individual distances for all members.

source	type	clusters covered	notes
Curtis et al. (2013)	classifier	Rup 147	
Douglas et al. (2014)	probability	Hyades, Praesepe	meta study
Bouy et al. (2015)	probability	M35	DANCe
Gonzalez (2016)	classifier	M67	
Rebull et al. (2016a)	members list	Pleiades	meta study
Rebull et al. (2017)	classifier	Praesepe	meta study
Douglas et al. (2017)	members list	Praesepe	meta study
Gaia Collaboration et al. (2018a)	members list	Hyades, M35, Rup 147, Pleiades, Praesepe	Gaia DR2, (1)
Cantat-Gaudin et al. (2018)	probability	M35, Rup147, Pleiades, Praesepe	Gaia DR2
Gao (2018)	probability	M67	Gaia DR2
Reino et al. (2018)	probability	Hyades	Gaia DR1, (1)
Olivares et al. (2018)	probability	Pleiades	Gaia DR2, DANCe
Olivares et al. (2019)	probability	Rup 147	Gaia DR2, DANCe

Notes. DANCe: DANCe membership study project. (1) Positions for Hyades were propagated to epoch 2000 using Gaia proper motions.

with

$$P_S(S|\lambda_1, \alpha, \sigma_S) = C \prod_{i=1}^M p(S_i|\lambda_1, \alpha, \sigma_{S,i}). \quad (\text{G.5})$$

890 C absorbs the normalization, or evidence term.

891 Following Wheatland (2004), we marginalize over λ_1 using the
892 δ function in G.4 to obtain

$$\begin{aligned} P_2(\lambda_2) &= \int_1^\infty d\alpha \cdot P_1\left(\lambda_2 \cdot \left(\frac{S_2}{S_1}\right)^{\alpha-1}\right) \cdot P_\alpha(\alpha) \\ &\cdot P_S\left(S|\lambda_2 \cdot \left(\frac{S_2}{S_1}\right)^{\alpha-1}, \alpha, \sigma_S\right) \end{aligned} \quad (\text{G.6})$$

893 Transforming P_S into a function of ϵ with $\lambda_1 = -\ln(1-\epsilon)/\Delta T$
894 yields:

$$\begin{aligned} P_S(S|\epsilon, \alpha, \sigma_S) &= C \prod_{i=1}^M p(S_i|\epsilon, \alpha, \sigma_{S,i}) \\ &= \frac{C}{\Delta T(1-\epsilon)} \\ &\cdot \prod_{i=1}^M \left[\frac{1}{2\pi\sqrt{\sigma_{S,i}}} e^{-\frac{\left(S_i - S_2 \left(\frac{-\ln(1-\epsilon)}{\Delta T\lambda_i}\right)^{1/(\alpha-1)}\right)^2}{2\sigma_{S,i}^2}} \right] \end{aligned} \quad (\text{G.7})$$

895 Finally, P_S enters the joint posterior distribution from Eq. 2, that
896 becomes

$$\begin{aligned} p(\epsilon, \alpha) &= C \cdot (-\ln(1-\epsilon)^M) \\ &\cdot (\alpha-1)^M \cdot \Gamma(\alpha) \left[\frac{(S_2/S_1)^{M+1}}{\pi} \right]^\alpha \\ &\cdot (1-\epsilon)^{(T/\Delta T) \cdot (S_2/S_1)^{\alpha-1}-1} \\ &\cdot P_S(S|\epsilon, \alpha, \sigma_S). \end{aligned} \quad (\text{G.8})$$

897

Table B.1. Non-exhaustive literature overview over OC parameters.

cluster	source	distance [pc]	age [Myr]	[Fe/H]
M35	adopted in this work:	861	$147.5 \pm^{13.5}_{13.5}$	-0.21 ± 0.10
M35	Bossini et al. (2019) ^a		$402.7 \pm^{13.5}_{0.9}$	
M35	Cantat-Gaudin et al. (2018)	861		
M35	Netopil et al. (2016)			-0.21
M35	Scholz et al. (2015)	830	151	
M35	Geller et al. (2010)		133	
M35	Meibom et al. (2009)		$147.5 \pm^{13.5}_{13.5}$	
M35	Bragaglia and Tosi (2006)	912		
M35	Steinhauser and Deliyannis (2004)			-0.143 ± 0.014
M35	Barrado (2001)		180	
M35	Barrado et al. (2001)			-0.21 ± 0.10
M35	Sung and Bessel (1999)	832		
Rup 147	adopted in this work:	305	$2650 \pm^{380}_{380}$	0.08 ± 0.07
Rup 147	Bragaglia et al. (2018)			0.08 ± 0.07
Rup 147	Cantat-Gaudin et al. (2018)	305		
Rup 147	Gaia Collaboration (2018)	309	$1995 \pm^{404}_{257}$	
Rup 147	Torres et al. (2018)	283	$2650 \pm^{380}_{380}$	
Rup 147	Curtis (2016) ^b			0.10 ± 0.02
Rup 147	Scholz et al. (2015)	270	1953	
Rup 147	Curtis et al. (2013)	300	$3125 \pm^{125}_{125}$	0.07 ± 0.03
Pleiades	adopted in this work:	135.6	$135 \pm^{25}_{25}$	-0.037 ± 0.026
Pleiades	Bossini et al. (2019) ^a		$86.5 \pm^{2.4}_{2.4}$	
Pleiades	Cantat-Gaudin et al. (2018)	135.6		
Pleiades	Gossage et al. (2018)		$135 \pm^{25}_{25}$	
Pleiades	Yen et al. (2018)	126.3	$141.3 \pm^{170}_{100}$	
Pleiades	Chelli and Duvert (2016)	139		
Pleiades	Netopil et al. (2016)			-0.01
Pleiades	Dahm (2015)		$112 \pm^{5}_{5}$	
Pleiades	Scholz et al. (2015)	130	120	
Pleiades	Conrad et al. (2014)			-0.037 ± 0.026
Pleiades	Melis et al. (2014)	136		
Pleiades	Bell et al. (2012)	135	125	
Praesepe	adopted in this work:	185.5	$750 \pm^{3}_{3}$	0.16
Praesepe	Bossini et al. (2019)		$750 \pm^{3}_{7}$	
Praesepe	Cantat-Gaudin et al. (2018)	185.5		
Praesepe	Gossage et al. (2018)		590	
Praesepe	Yen et al. (2018)	183	$794 \pm^{253}_{269}$	
Praesepe	Netopil et al. (2016)			0.16
Praesepe	Scholz et al. (2015)	187	832	
Praesepe	Boesgaard et al. (2013)			0.12
Praesepe	Boudreault et al. (2012)	160	630	
Praesepe	Salaris et al. (2004)	175	650	
M67	adopted in this work:	908	$3639 \pm^{17}_{17}$	$-0.102 \pm .081$
M67	Bossini et al. (2019)		$3639 \pm^{17}_{17}$	
M67	Netopil et al. (2016)			0.03
M67	Scholz et al. (2015)		$3428 \pm^{147}_{72}$	
M67	Conrad et al. (2014)			$-0.102 \pm .081$
M67	Dias et al. (2012)	908	4300	
M67	Oñehag et al. (2011)	880	4200	0.02
Hyades	adopted in this work: ^c		$690 \pm^{160}_{100}$	0.13 ± 0.02
Hyades	Gaia Collaboration (2018)		$690 \pm^{160}_{100}$	
Hyades	Gossage et al. (2018)		680	
Hyades	Liu et al. (2016)			± 0.02
Hyades	Netopil et al. (2016)			0.13
Hyades	Taylor and Joner (2005)			0.103 ± 0.008
Hyades	Cummings et al. (2005)			0.146 ± 0.004
Hyades	Salaris et al. (2004)		650	0.15
Hyades	Perryman et al. (1998)		$625 \pm^{50}_{50}$	
Hyades	Martin et al. (1998)		$650 \pm^{70}_{70}$	

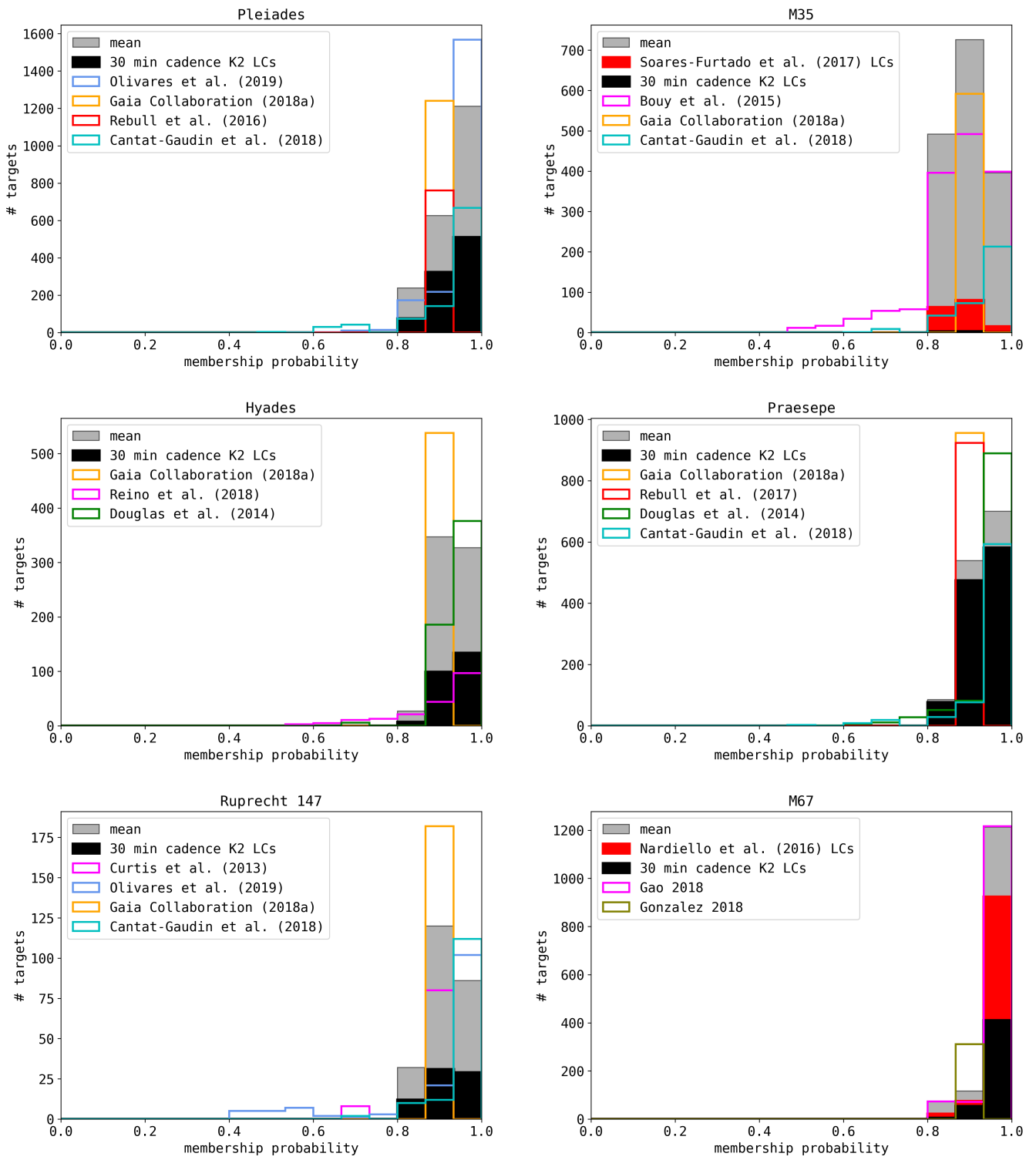


Fig. A.1. Membership histograms.

Table F.1. Literature overview over power law fitting approaches to FFDs.

Who	method	data	$\alpha - 1$
Hawley et al. (2014)	LSq with Poisson uncertainty, increase the low energy limit until the fit is robust		.95 (binned), 1.01 (cumulative)
Davenport (2016)	weighted LSq, asymmetric Poisson confidence intervals following Gehrels1986		
Gizis (2017)	de-biased MLE (Arnold2015), weight each point with $\text{sqrt}(N)$ in each bin (Clauset+2009)	22 flares on one M7 UCD	.6-1. (31-33 erg)
Paudel et al. (2018)	ML from a paper in 2010, used emcee (Foreman-Mackey2013)		
Lacy (1976)	graphical, linear LSq	386 flares on UV Cetis	.43-1.
Güdel et al.(2003)	-		
Davenport et al. (2012)	Fit $\log_{10} Y = \alpha + (\beta \log_{10} X)(10 - \gamma/(X + \delta))$	~50,000 M dwarfs from SDSS and 1321 M dwarfs from 2MASS	.9-2.1
Lurie et al. (2015)	Bayesian Markov chain Monte Carlo based algorithm (Kelly 2007) for linear regression	2 dMe5 dwarfs	.92-1.03
Audard et al. (2000)	Crawford+1970 MLE (Jauncey-style)	EUVE 12 F-M type stars, 10-20 flares each	.46-1.61
Shakhovskaia (1989)	linear representation, power laws from Gershberg/Shakhovskaya1983	30-40 dK0-dM8, 200 flares	.4-1.4
Yang et al. (2017)	binned FFDs	103187 flares on 540 M-type dwarfs in Kepler	1.07 +/- 0.35
Howard et al. (2018)	fit a cumulative power law, MCMC for uncertainties	575 flares on 284 stars	0.84-1.34
Hilton et al. (2011)			.63-.83